Journal of Energy Storage 76 (2024) 109757

Contents lists available at ScienceDirect

Journal of Energy Storage

journal homepage: www.elsevier.com/locate/est

Research papers

Preparation of g-C_3N_4/ZIF-8/PVDF–modified Li anode for all-solid-state Li metal batteries

Kumlachew Zelalem Walle [a,b,c], Yi-Shiuan Wu [a], She-Huang Wu [d], Wen-Chen Chien [b], Jeng-Kuei Chang [g], Rajan Jose [e], Chun-Chen Yang [a,b,f,*]

[a] Battery Research Center of Green Energy, Ming Chi University of Technology, New Taipei City 24301, Taiwan, ROC
[b] Department of Chemical Engineering, Ming Chi University of Technology, New Taipei City 24301, Taiwan, ROC
[c] University of Gondar, Department of Chemistry, Gondar, Ethiopia
[d] Graduate Institute of Science and Technology, National Taiwan University of Science and Technology, 43, Sec. 4, Keelung Road, Taipei 106, Taiwan, ROC
[e] Nanostructured Renewable Energy Materials Laboratory, Faculty of Industrial Sciences and Technology, University Malaysia Pahang, 26300 Kuantan, Malaysia
[f] Department of Chemical and Materials Engineering, and Green Technology Research Center, Chang Gung University, Taoyuan City 333, Taiwan, ROC
[g] Department of Materials Science and Engineering, National Yang Ming Chiao Tung University, 1001 University road, Hsinchu, 30010, Taiwan, ROC

ARTICLE INFO

Keywords:
High-voltage cathodes
Hybrid solid electrolytes
Garnet
Graphitic-carbon nitride (g-C_3N_4)
ZIF-8 MOF

ABSTRACT

All-Solid-state lithium metal batteries (ASSLMBs) are promising next-generation energy storage devices. However, the formation of lithium (Li) dendrites in ASSLMBs limits their applications. In this study, we used an inorganic/organic mixture of graphitic carbon nitride (g-C_3N_4), zinc-based Zeolitic Imidazolate Framework-8 (ZIF-8), and poly(vinylidene difluoride) (PVDF)—g-C_3N_4/ZIF-8/PVDF (g-CNZP)—to modify the surface of a lithium metal anode (LMA). The 2032-type coin cell was assembled based on a lithium Nafion (LiNf)–coated NCM811 (denoted as LiNf@NCM811) cathode, inorganic/organic mixture modified Li metal anode (LMA) (denoted g-CNZP@Li), and a LiNf-coated $Li_{6.05}Ga_{0.25}La_3Zr_2O_{11.8}F_{0.2}$ ($LiNf@LG_{0.25}LZOF$) filler in bilayer hybrid solid electrolyte (Bi-HSE). The coin cell was charged between 2.8 and 4.2 V at 0.5C exhibited an initial specific discharge capacity of 134.45 mAh g^{-1} and retained 86.1 % of its capacity after 280 cycles at 30 °C. The average coulombic efficiency of the cell was approximately 99.8 %. Furthermore, the high-voltage (2.8–4.5 V, at a rate of 0.2C) result also delivered an initial specific discharge capacity of 194.3 mAh g^{-1} and, after 100 cycles, maintained 81.8 % of its initial capacity at room temperature. The presence of the nanosheet/nanoparticle composite coating material on the LMA surface suppressed Li dendrite growth and enhanced the compatibility between the LMA and Bi-HSE membrane. In addition, the *in-situ* formation of Li_3N on the solid electrolyte interface (SEI) layer improved the ionic conductivity and ensured intimate interfacial contact during cycling. Therefore, these novel bi-layered fabrication strategies for obtaining hybrid/composite solid electrolyte membranes and modifying LMA surfaces *via* 2D g-C_3N_4 material with ZIF-8 MOFs and PVDF composites appear to have applicability in the preparation of very safe high-voltage cathodes for ASSLMBs.

1. Introduction

With their long cycle lives and high energy densities, lithium-ion batteries (LIBs) have received much attention as alternatives to conventional energy storage systems. Because conventional liquid electrolyte battery systems can be highly flammable and susceptible to liquid leakage, solid-state electrolytes (SSEs) have promise for improving the safety of LIB systems [1]. SSEs appear in many forms, including solid polymer electrolytes (SPEs), inorganic solid electrolytes (ISEs), and hybrid/composite polymer electrolytes (HSEs) [2]. SPEs comprise a polymer matrix mixed with lithium salts; consequently, they are easy to process, have good flexibility and offer safe performance and good interfacial contact with electrodes [3,4]. Nevertheless, SPEs exhibit low ionic conductivity, inferior thermal and electrochemical stabilities, and unsatisfactory behavior in their ability to suppress lithium dendrite growth. In comparison, ISEs display higher ionic conductivities, a wide electrochemical window, and high mechanical strength, but provide poor interfacial contact with electrodes [4,5]. These various disadvantages of SPEs and ISEs severely restrict their commercial applications in powering lithium batteries. HSEs constructed from SPEs and inorganic

* Corresponding author at: Battery Research Center of Green Energy, Ming Chi University of Technology, New Taipei City 24301, Taiwan, ROC.
E-mail address: ccyang@mail.mcut.edu.tw (C.-C. Yang).

https://doi.org/10.1016/j.est.2023.109757
Received 5 September 2023; Received in revised form 8 November 2023; Accepted 14 November 2023
Available online 22 November 2023

fillers can benefit from the attractive features of their components to ensure high ionic conductivity, good flexibility, and intimate contact with electrodes [6].

Among the various ISE candidates, garnet-type ($Li_7La_3Zr_2O_{12}$) SSEs have the lowest reduction potential (0.05 V) and least favorable decomposition reaction energy, making them chemically and electrochemically stable toward Lithium metal anodes (LMAs) [7]. Although Li metal is one of the best anode materials for rechargeable batteries (because of its low standard electrode potential and high theoretical capacity), its interfacial instability and the inevitability of dendrite formation on its surface limit the practical applications of Li metal in commercial batteries [8]. Many attempts have been made to develop effective methods to solve these problems, with surface modification of Li metal being one of the most commonly used [9,10]. The lithiophobic nature of garnet toward the surface of Li metal results in inadequate contact and high interfacial resistance [11]. Hence, Li metal surface coating materials are required to ensure lithiophilicity. Based on the types of the materials being coated and the structures of the coating layers, *ex-situ* coating can be classified into organic monolayer coating, inorganic monolayer coating, hybrid organic/inorganic monolayer coating, and multilayer coating [12]. Organic protective layers [13] that possess excellent toughness [*e.g.*, poly(vinylidene difluoride) (PVDF), [14] porous polydimethylsiloxane (PDMS)] can be used directly as protective layers to suppress the growth of Li dendrites [15]. Such coating layers can automatically adjust their strength through a change in strain, thereby accommodating Li deformation and decreasing the extent of side reactions. On the other hand, inorganic protective layers possess high mechanical moduli and fast Li-ion diffusion conductivities [16]. An ideal solid electrolyte interphase (SEI) would display all of these properties simultaneously, but in practice it is difficult to combine both organic and inorganic protective layers to meet the requirements of an advanced SEI. Therefore, hybrid protective layers, fabricated from rational combinations of organic and inorganic materials, are expected to synergistically exert their respective functions and satisfy the properties of an ideal artificial SEI [12].

Various strategies have been tested to realize good interfacial contact between the LMA and the electrolyte surface, including coating the LMA with a thin surface layer of Al_2O_3 [17], graphite [18], ionic liquid [19], Li_3N [20], ZnF_2 [21], $AgNO_3$ [22], graphitic carbon nitride (g-C_3N_4) [23], and metal–organic frameworks (MOFs) [24]. Some efforts have been devoted toward improving the Li metal–garnet interface. According to recent reports [25,26], g-C_3N_4 can function as an effective ion transport medium in SSEs. For example, Huang et al. demonstrated that introducing g-C_3N_4 into Li metal ensured intimate contact at the interface between Li metal and garnet-type SSE and suppressed Li dendrite formation relative to that of the pristine Li metal [23]. A Li-ion conducting compound, Li_3N that forms *in-situ* at the Li–solid electrolyte interface can also effectively conduct Li-ions and suppress Li dendrite growth [23,27–29]. Luo et al. found that a thin (*ca.* 4 μm) and highly polar β-phase PVDF coating functioned as an efficient artificial SEI for the effective suppression of Li dendrite formation and for enhancing the high-rate cyclability of the LMA [14]. Recently developed composite SSEs have been designed using metal organic frameworks (MOFs); these materials, synthesized by assembling metal ions with organic ligands, have high surface areas, abundant micropores, excellent thermal and electrochemical stabilities, and open channels after absorbing Li-ion conductors or inorganic fillers in polymer electrolytes [24]. The SSEs that contained ZIF-8 also displayed improved ionic conductivity and mechanical strength, which inhibited Li dendrite growth. In addition, the zinc metal and 2-methylimidazole ligands coordinated in the framework structure of the ZIF-8 nanoparticles that were incorporated into the composite coating material inhibited dendrite growth and enhanced the affinity of the coating material toward Li-ion conductors. Similarly, the ZIF-8 cages not only interacted with small solvent molecules but also ensured that Li-ions had access to continuous channels of transport and good contact with the electrodes. As a result of their pores and interactions with guest molecules, MOFs can be effective at controlling the dynamics of and interactions with small molecules [24,30].

In this study, we prepared a suspension of g-C_3N_4, zinc-based Zeolitic Imidazolate Framework-8 (ZIF-8), and PVDF in *N*,*N*-dimethylformamide (DMF) and used it as a hybrid inorganic/organic monolayer coating material denoted as graphitized Carbon Nitride Zeolitic Polymer (g-CNZP) for an LMA, which was subsequently dried at 80 °C for 1 h in a glove box. The charge/discharge electrochemical operation forms Li_3N, which has a good Li-ion conducting property. This *in-situ* formation of Li_3N on Li anode greatly improves the intimate contact between Li–bilayer hybrid solid electrolyte (Bi-HSE) interface and can also effectively suppress Li dendrite growth.

2. Experimental section

2.1. Chemicals

The following precursor materials were used to prepare Ga and F dual doped $Li_7La_3Zr_2O_{12}$ (LLZO); Lithium hydroxide monohydrate (98 %, Alfa Aesar), Lantanum nitrate hexahydrate (99.9 %, Alfa Aesar) Zirconium oxychloride octahydrate (99.9 %, Sigma-Aldrich), Active Ingredient nitrate hydrate (99.9 %, Alfa Aesar), Ammonium hydroxide (30–33 %, Fluka) and Sodium hydroxide (98 %, Fluka). The polymeric Li-ion conducting coating material, Lithium nafion prepared from Nafion (5 wt% in H_2O and 1-propanol, Sigma-Aldrich) solution. g-C_3N_4 was ob-tained from calcination of Melamine (Sigma-Aldrich) and for further exfoliation Nitric acid (70–71 %, AENCORE) was used. To synthesize ZIF-8 MOF, Zinc nitrate hexahydrate (≥98 %, Sigma-Aldrich), and 2- methylimidazole (99 %, Sigma-Aldrich) were used. The Bi-HSE com-posite membrane was prepared from poly(vinylidenefluoride-*co*-hexa-fluoropropylene) (Sigma-Aldrich, Mw = 400,000), Lithium bis (trifluoromethanesulfonimide) (99.95 %, Sigma-Aldrich) and Succino-nitrile (99 %, Sigma-Aldrich). Different solvents such as Ethanol (≥99.8 %, Sigma-Aldrich), Methanol (99.8 %, Duksan), *N*, *N*-dimethylforma-mide (≥99.8 %) have been used for the preparation of materials. All the chemicals were used without further purification.

2.2. Material synthesis

2.2.1. $LG_{0.25}LZOF$ ceramic electrolytes

After collecting the mixed metal hydroxide precursor [$La_3Zr_2Ga_{0.25}(OH)_y$] from a Taylor flow reactor, as described in our previous work [31], the dual-doped Li garnet $Li_{6.05}Ga_{0.25}La_3Zr_2O_{11.8}F_{0.2}$ (abbreviated herein as $LG_{0.25}LZOF$) material was fabricated by mixing the dried $La_3Zr_2Ga_{0.25}(OH)_y$ precursor powder with a stoichiometric amount of $LiOH{\cdot}H_2O$ and for the fluoride source LiF was added. A 10 mol% excess of $LiOH{\cdot}H_2O$ was added to compensate for possible Li loss during sintering at high temperature. The mixtures were then ball-milled in a methanol solution for 20 min. After drying, the mixed powder was sintered at 900 °C for 2 h at a heating rate of 3 °C min^{-1} in an air oven. Finally, the resultant ceramic powder was sieved and stored in an Ar-filled glove box where the oxygen and moisture level were <0.5 ppm.

2.2.2. Few-layer g-C_3N_4 from melamine

Bulk g-C_3N_4 was prepared by directly heating melamine powder (5.0 g) in a furnace for 4 h at 550 °C. The as-prepared bulk g-C_3N_4 (1 g) was then mixed with HNO_3 (70 wt%, 30 mL) and stirred for 5 h at room temperature, as schematically illustrated in Fig. S1 (Supporting Infor-mation). The resulting mixture was poured slowly into deionized water (200 mL) and sonicated for exfoliation, with the temperature of the system controlled between 60 and 80 °C. To remove any unexfoliated g-C_3N_4, the suspension was centrifuged (8500 rpm), washed with deion-ized water and ethanol, and dried at 80 °C. The nanosheet few-layered g-C_3N_4 powder was obtained after dispersing in ethanol and homoge-nizing using a Nano Genizer (LLC, USA).

2.2.3. ZIF-8 nanoparticles

Solutions of zinc nitrate hexahydrate [$Zn(NO_3)_2{\cdot}6H_2O$] and 1,2-dimethylimidazole were prepared separately in methanol with a molar ratio of 1:5. The copolymerization was performed by pouring the 2-methylimidazole solution slowly into the container of Zn^{2+} solution under constant stirring at room temperature. The white precipitate (ZIF-8) was collected by centrifugation (8000 rpm, 10 min), washed three times with methanol, and dried in an oven at 60 °C overnight [32].

2.2.4. Preparation of composite coating material for Li metal modification

Inorganic/organic composite coating slurry material was formulated in accordance with the procedure depicted in Scheme 1. Initially, the 2D nano-sheet g-C_3N_4 (1 wt%) and ZIF-8 nanoparticle (1 wt%) powders were introduced into a sample vial containing *N*,*N*-dimethylformamide (DMF) solvent. Subsequently, the mixture was subjected to ultra-sonication for a duration of 2 h to ensure homogeneous dispersion. Following this, PVDF (2 wt%) powder was incorporated into the system and stirred overnight at a temperature of 60 °C. Then the pristine Li foils were coated and subjected to a drying process at 80 °C for 1 h in an enclosed environment, H_2O and $O_2 < 0.5$ ppm.

2.2.5. Bilayer hybrid solid polymer electrolyte membrane

The bilayer composite solid electrolyte membrane was prepared by varying the filler content while following previously reported solution-casting procedures [31,33]. Poly(vinylidene fluoride–*co*–hexafluoropropylene) (PVDF-HFP), succinonitrile (SN, 20 wt% *vs.* polymer), and LiTFSI (1:1 *vs.* polymer) were dissolved in DMF in two different vials. The solutions were stirred magnetically at 60 °C until all the components had dissolved completely. The mixture of the three components namely PVDF-HFP + LiTFSI + SN is denoted as SPE. Lithium Nafion (LiNf)–coated $Li_{6.05}Ga_{0.25}La_3Zr_2O_{11.8}F_{0.2}$ ($LiNf@LG_{0.25}LZOF$) filler was dispersed well in DMF and added into the two solutions, with stirring continuing for 6 h. After the incorporation of $LiNf@LG_{0.25}LZOF$ filler in to SPE mixture, it is designated as Bi-HSE. The LiNf coating step has been described previously [31]. The first homogenous solution (20 wt% ceramic filler *vs.* polymer) was cast into a glass plate, followed by the second solution (80 wt% ceramic filler *vs.* polymer). The mixture was vacuum-dried at 60 °C for 48 h and then at 80 °C for 48 h to remove any residual DMF. Subsequently, cold pressing (1500 psi, 3 min) was performed to squeeze out the remaining DMF solvents and to achieve uniform and bubble-free HSEs having thicknesses in the range of 140–150 μm. The as-prepared dried HSE films were punched into discs (diameter: 18 mm) and stored in a glove box (MBraun, Germany) filled with Ar gas ($O_2 < 0.5$ ppm; $H_2O < 0.5$ ppm).

2.2.6. LiNf@NCM811 composite cathode material

The $LiNi_{0.8}Co_{0.1}Mn_{0.1}O_2$ (NCM811) cathode material was obtained from Green Eco-Manufacture. The NCM811 cathode was coated by lithium nafion (LiNf), Li-ion conducting polymer. The preparation of LiNf and coating procedure of the NCM811 cathode material is described in our previous work [31]. The Lithium nafion coated NCM811 is denoted as LiNf@NCM811. The composite cathode slurry was prepared by mixing LiNf@NCM811, LiTFSI, Super-P, vapor grown carbon fiber (VGCF), and PVDF (80:4:8:1:7, wt%) in DMF. The mixture was agitated for 4 h to form uniform slurry and then coated on a carbon-coated aluminum foil current collector. The composite cathode was dried overnight at 80 °C and then at 120 °C for 6 h, cut into circular discs (ϕ = 13 mm) for coin cell assembly. The active material loading of LiNf@NCM811 in the composite cathode was approximately 4.5 mg cm^{-2}. The charge and discharge testing of the batteries were performed between 2.8 and 4.2 V and 4.5 V at 30 °C and room temperature, respectively.

2.3. Materials characterization

The crystal structures of the as-prepared powder and membranes were characterized through X-ray diffraction (XRD; Bruker D2 PHASER, Germany; Cu Kα; $\lambda = 0.15406$ nm; 30 kV, 10 mA) for angles in the range of 10–80°. The functional groups and the chemical environments of the elements in the as-prepared bulk and few-layered g-C_3N_4 powders were identified using Fourier transform infrared (FTIR) spectroscopy (Spectrum100, PerkinElmer, USA). Scanning electron microscopy (SEM; Hitachi Se2600H, Japan) was used to study the microstructures of the as-prepared powder, HSE electrolyte membranes, and pristine/modified Li foil. The binding energies and elemental valences in the pristine and coated Li electrode after cycling were investigated using X-ray photoelectron spectroscopy (XPS, Sigma Probe, Thermo VG–Scientific, UK; X–ray source: Al K–alpha 1486.6 eV) with XPSPEAK software (v. 4.1). All XPS spectra were normalized based on C 1s, C—C peak at 284.8 eV. To prevent air or moisture contamination, the samples were transferred from glovebox to XPS or SEM instruments using vacuum transfer box container filled with an Ar gas. The thermal stabilities of the powder and HSE electrolyte membranes were investigated through thermogravimetric analysis (TGA; Mettler Toledo, USA) under N_2 at temperatures from 25 to 700 °C at a heating rate of 10 °C min^{-1}. The *in-situ* gas generations behaviors during cycling were investigated by differential electrochemical mass spectrometry (DEMS, UK).

2.4. Electrochemical performance measurements

The electrochemical cycling performance of the PVDF-HFP/garnet–based solid electrolyte (Bi-HSE) battery was assessed using a CR2032 coin-type cell. The solid-state batteries were assembled in a glove box filled with Ar; they featured a positive electrode (Ø = 13 mm), a Bi-HSE membrane disk (Ø = 18 mm), and a negative electrode (Ø = 15 mm). Charge/discharge tests were performed over the voltage range

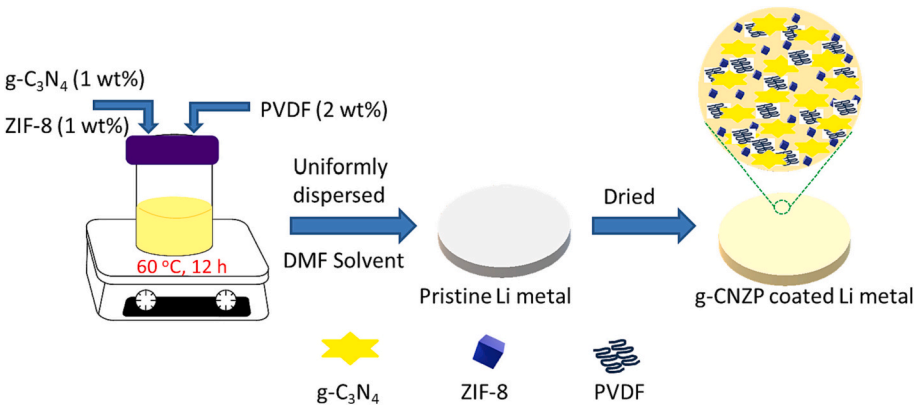

Scheme 1. Preparation of composite coating material (g-CNZP) and modification of Li metal anode.

2.8–4.2 and 4.5 V using a AcuTech Battery Testing Systems. AC impedance (PGSTAT302N, MetrOhm Autolab B. V., Netherlands) was measured over the frequency range from 1 MHz to 100 mHz with an amplitude of 5 mV.

The ionic conductivity of the Bi-HSE solid electrolyte was measured using electrochemical impedance spectroscopy (EIS) with a controlled-environment sample holder (CESH; Biologic Instruments, France) Au as a blocking electrode with the configuration of Au/Bi-HSE/Au. The frequency range was fixed from 1 MHz to 100 mHz at a step size of 10 °C between 30 and 80 °C. *Prior* to measurement, the samples were stabilized at the particular measuring temperature for 2 h in a CESH holder (Biologic, France). The ionic conductivity of the Bi-HSE membrane was calculated by Eq. (1):

$$\sigma = L/(RA) \quad (1)$$

where L is the thickness (cm) of the Bi-HSE membrane, R is the impedance (Ω), and A is the contact area (cm^2) of the electrolyte and the electrode.

The electronic conductivity was determined from the I-V curve using CESH holder (Biologic, France). Linear sweep voltammetry (LSV; PGSTAT302N, MetrOhm Autolab B. V., Netherlands) of the Bi-HSE membrane with pristine and g-CNZP–coated Li was performed with a cell configuration of g-CNZP@Li(Li)/Bi-HSE/Stainless steel (SS) between a voltage window of 1–6 V at a scan rate of 1 mV s^{-1}.

3. Results and discussion

3.1. Microstructure and morphology

We used XRD to examine the as-prepared Bi-HSE membrane and g-C_3N_4 powder before and after exfoliation and ZIF-8 powder, as shown in Fig. 1(a). The composite electrolyte membranes were synthesized using a simple solution-casting process. The as-prepared $LG_{0.25}$LZOF powder applied in the HSEs possessed the crystal structure of a pure cubic phase, similar to that of standard cubic-LLZO (PDF 00-063-0174, LLZO), which is the conductive phase of LLZO. The XRD patterns revealed that the crystallinity of LiNf@$LG_{0.25}$LZOF did not change after it was embedded in a PVDF-HFP polymer matrix, suggesting that LiNf@$LG_{0.25}$LZOF and PVDF-HFP had good compatibility during the preparation process. The pattern of the pristine PVDF-HFP film featured two crystalline peaks with values of 2θ of 18.8 and 20.2°, with a relatively weak peak in the range 30–45°, indicating that the ordered arrangement of the pure

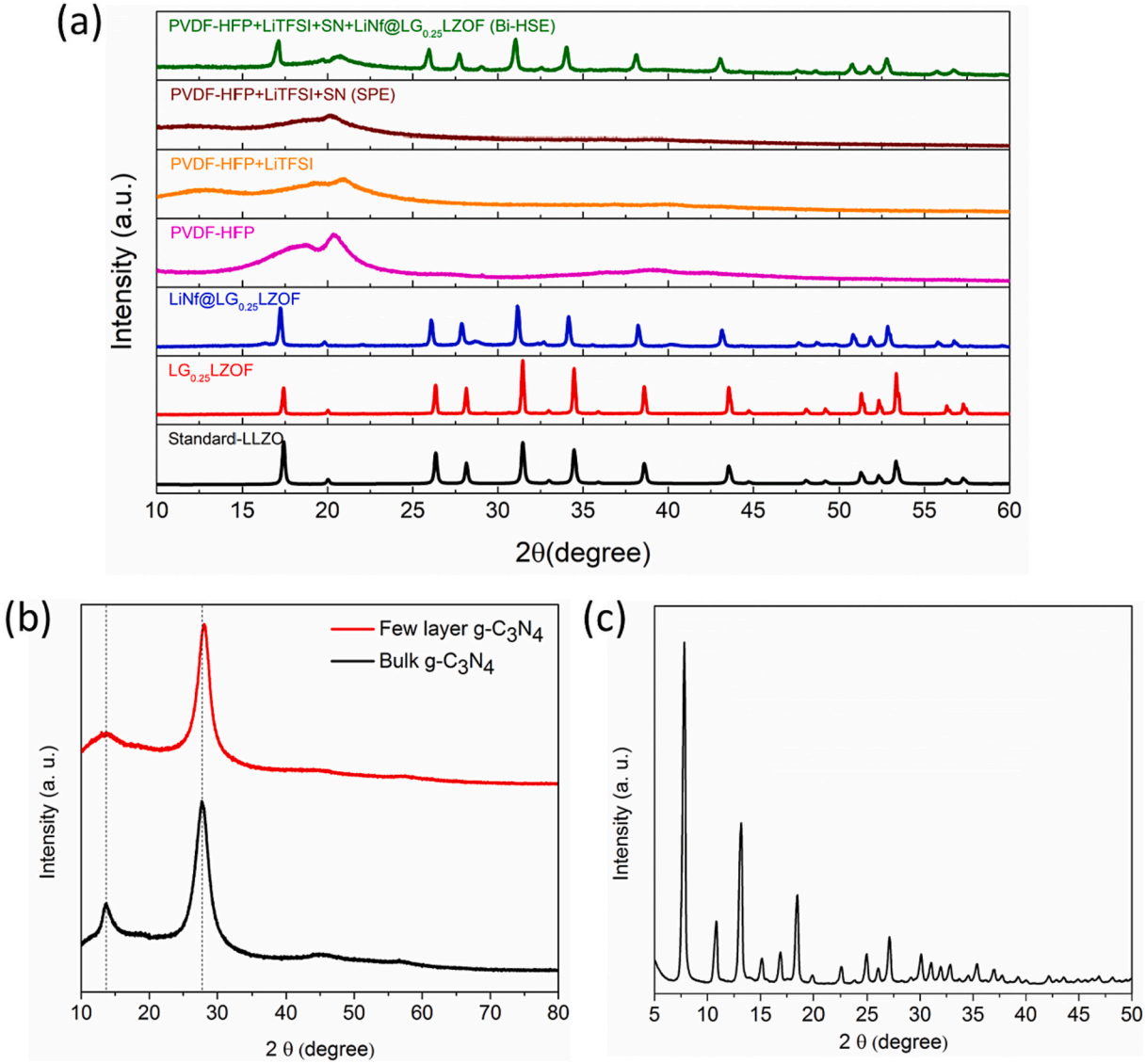

Fig. 1. XRD patterns of (a). The $LG_{0.25}$LZOF powder and the components of Bi-HSE composite solid electrolyte membrane, and (b). Bulk and few-layered graphitic-C_3N_4, (c). ZIF-8 powder.

copolymer film led to its highly crystalline phase. After the LiTFSI salt, SN plasticizer, and LiNf@$LG_{0.25}$LZOF filler had been added successively, the intensities of those two peaks in the patterns of the PVDF-HFP + LiTFSI + SN (denoted as SPE) and PVDF-HFP + LiTFSI + SN + LiNf@$LG_{0.25}$LZOF (hereafter denoted as Bi-HSE) membranes were much weaker, indicating that the degrees of crystallinity of the polymer had decreased markedly [34].

Fig. 1(b) presents the crystalline structures of the as-prepared light-yellow powders of bulk g-C_3N_4 and few layered g-C_3N_4 after acid treatment and exfoliation using a Nanogenizer device. We assign the main peak observed at a value of 2θ of 27.8° to the (002) plane, representing the distance between the layers of the graphitic material in the bulk g-C_3N_4. We attribute the peak at a value of 2θ of 13.7° to the (100) plane, representing the intralayer *d*-spacing [35]. Two broad peaks at 27.8° (002) and 13.7° (100) correspond to the interplanar spacings in the tri-*s*-triazine unit and the conjugated aromatic system structures of the g-C_3N_4 powder. The corresponding signal for the (100) plane of the few-layer g-C_3N_4 at a value of 2θ of 13.7° was much weaker than that of the bulk g-C_3N_4, due to the decrease in the planar size of the layers after exfoliation. Meanwhile, the signal for the (002) plane had moved from 27.8° for the bulk g-C_3N_4 to 28.1° for the few-layered g-C_3N_4, because of the shorter distance between the single sheets.

The phase structure of ZIF-8 powder was determined by XRD. The XRD pattern of ZIF-8 as shown in Fig. 1(c) is identical to the presented patterns, confirming the successful synthesis of the material [1]. Based on literature review, the characteristic diffraction peaks of ZIF-8 sodalite (SOD) structures are at 2θ = 7.8°, 10.8°, 13.1°, 15.1°, 16.8°, 18.4°, 22.5°, 24.9°, 27.1° and 30.1° for ZIF-8 sample were clearly observed in Fig. 1(c), which can be assigned to (011), (002), (112), (022), (013), (222), (114), (233), (134) and (044) planes respectively. Our data confirm the good crystallinity of ZIF-8 material synthesized phases without any side product.

Fig. 2(a) displays the SEM image of the bulk g-C_3N_4 powders obtained after calcination of melamine powder. After treatment with HNO_3, the bulk g-C_3N_4 powder provided the few-layer g-C_3N_4, as displayed in Fig. 2(b). Further exfoliation using a homogenizer resulted in the sheet-like morphology of few-layered g-C_3N_4, as depicted in Fig. 2(c). The high-magnification TEM image in Fig. 2(d) reveals that the homogenized g-C_3N_4 from the Nanogenizer possessed a nanosheet morphology. The elemental compositions of the few-layered g-C_3N_4 nanosheets were obtained through EDX mapping. The measured atomic-percentage compositions of the few-layered g-C_3N_4 revealed that it contained mainly carbon (*ca.* 45.4 %) and nitrogen (*ca.* 54.6 %) [Fig. 2(e)]. The SEM image of ZIF-8 is displayed in Fig. 2(f), demonstrating that

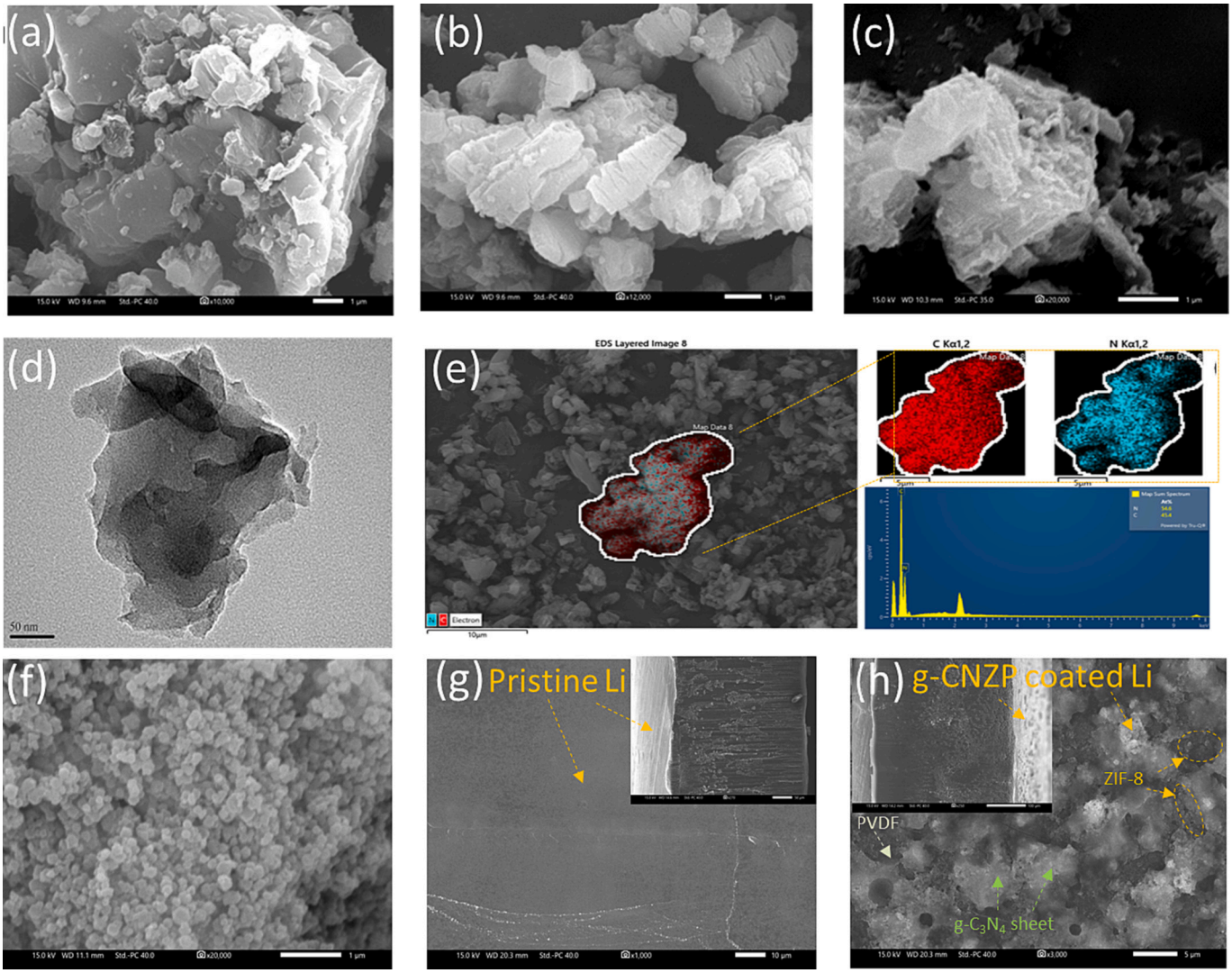

Fig. 2. SEM images of (a). Bulk g-C_3N_4; few-layered g-C_3N_4, (b). After acid treatment, (c). After nanogenizer processing, (d). TEM image of homogenized few-layered g-C_3N_4, (e). EDX mapping of g-C_3N_4, SEM image of (f). ZIF-8, (g). Pristine Li (inset view: cross-sectional image) and (h) g-CNZP Modified Li (inset view: cross-sectional image) before cycling.

the particle dimensions are smaller than 100 nm. Fig. 2(g) and Fig. 2(h) depict, respectively, both the pristine and the g-CNZP coated Lithium metal anode (LMA). The modified Li metal anode exhibits a visible presence of composite coating materials on its surface. The two-dimensional sheet-like structure of g-C_3N_4 effectively covers the surface of the Li metal anode, with the assistance of PVDF polymer, enabling the interconnection of ZIF-8 nanoparticles with g-C_3N_4 and their firm adhesion to the surface of the Li anode. Moreover, these composite coating materials enhance compatibility with the bilayer hybrid electrolyte membrane while simultaneously suppressing the growth of lithium dendrites. This phenomenon facilitates an intimate contact between the LMA and the solid electrolyte membrane using the composite coating materials as an adhesive agent, ultimately enhancing the long-term cycling performance of the cell, particularly at higher cut-off voltages.

Fig. 3(a) displays the FTIR spectrum of the melamine-derived g-C_3N_4. We assign the peak at 808 cm^{-1} to the typical bending vibrations of tri-*s*-triazine units and that at 886 cm^{-1} to the deformation mode of N—H bonds. The broad absorption band near 3200 cm^{-1} represented the stretching vibrations of N—H bonds, associated with uncondensed amino groups. A series of distinctive characteristic absorption peaks appeared in the range 1650–1240 cm^{-1}, including a peak at 1640 cm^{-1} for C═N stretching vibration modes and peaks at 1569, 1412, 1323, and 1243 cm^{-1} associated with heterocycle C—N stretching [23,27,28].

Fig. 3(b) reveals the thermal stability of the LiNf@$LG_{0.25}$LZOF powder and the as-prepared SPE and Bi-HSE membranes. The thermal decomposition temperature of the Bi-HSE composite membrane (*ca.* 360 °C) was higher than that of the SPE (*ca.* 327 °C). We ascribe the first weight loss of the electrolyte membrane (up to 100 °C) to the release of trapped moisture and residual solvent from the membrane. The second stage of weight reduction, which is approximately from 150 to 320 °C, is mainly due to the decomposition of the SN plasticizer and melting and gradual degradation of the PVDF-HFP copolymer. Thermal decomposition of the copolymers and the Li salt (LiTFSI) in the bilayer HSE membrane began at approximately after 350 °C, possibly due to the presence of LiNf@$LG_{0.25}$LZOF filler, which can assist the composite membrane for further thermal stability [36,37]. Increasing the temperature to 700 °C led to a residual weight of Bi-HSE of approximately 37 %; that of the SPE was only approximately 22 %. Therefore, the incorporation of the LiNf@$LG_{0.25}$LZOF ceramic fillers improved the thermal stability of the composite membranes for solid-state Li-metal battery (LMB) applications.

Most commercial LIBs have a working voltage range up to approximately 4.0–4.3 V. The polymer electrolyte must be chemically inert within the operating voltage window. Thus, the oxidation potential of the SSE should be at least 4.3 V to prevent electrolyte decomposition or oxidation. We measured the electrochemical stability window (ESW) of our Bi-HSE composite membrane in the coin cell with the configuration Li/Bi-HSE/SS, using the pristine and g-CNZP–coated LMAs, through LSV from 1.0 to 6.0 V at a scan rate of 1 mV s^{-1} at room temperature. As displayed in Fig. 4(a), the current response of the g-CNZP@Li/Bi-HSE/SS cell was stable relative to that of the pristine one, with the voltage range reaching up to approximately 5.0 V (*vs.* Li/Li^+). Notably, the pristine-Li anode cell exhibited a slight onset of voltage at 4.15 V (*vs.* Li/Li^+) in the LSV plot. The improved electrochemical stability for Bi-HSE with the g-CNZP coated Li (g-CNZP@Li/Bi-HSE/SS) cell can be attributed to the incorporation of the coating materials. The 2D g-C_3N_4 nanosheet morphology and ZIF-8 nanoparticle demonstrate high stability to Li metal. Furthermore, the presence of strong oxidation resistance PVDF binder in the coating material may also improve its stability toward Li. The thin coating layer on the Li surface can effectively mitigate the decomposition of Bi-HSE electrolyte membrane at higher upper voltage, improve the electrochemical stability window of electrolyte, and is beneficial to the long-term stable cycle of the battery. The improved electrochemical stability of the g-CNZP@Li/Bi-HSE/SS cell over a wider voltage range indicates that our as-prepared composite membrane could meet the requirements of most high-voltage cathode materials.

We determined the ionic conductivity of the Bi-HSE composite membrane at various temperatures in the range from 30 to 80 °C with a step size of 10 °C. The room-temperature total ionic conductivity, calculated based on Eq. (1), was approximately 6.8×10^{-4} S cm^{-1}. The Nyquist spectra in Fig. 4(b) reveal that the composite membrane electrolyte exhibited an ionic conductivity of 9.4×10^{-4} S cm^{-1} at 80 °C. The thickness of the composite membrane was approximately in the range 140–150 μm. The SEM cross-sectional view of the Bi-HSE membrane is shown in Fig. S2(a). The electronic conductivity of Bi-HSE membrane was obtained from *I*–V plot of DC polarization measurement, as exhibited from Fig. S2(b). The Bi-HSE membrane was assembled within the confines of the Controlled Environment Sample Holder (CESH) for the purpose of ascertaining the intrinsic electrical conductivity (σ_e). The room temperature σ_e value of Bi-HSE membrane is approximately 1.6×10^{-7} S cm^{-1}, which exhibits a notable discrepancy when compared to its corresponding ionic conductivity ($\sigma_i = 6.8 \times 10^{-4}$ S cm^{-1}) measured at the same condition. It indicates that the as-prepared bilayer membrane sample is ionic conductors and electronic insulators by nature. We varied the current densities to investigate the effect of the g-C_3N_4/ZIF-8/PVDF composite coating material on Li anode for the electrochemical performance of symmetrical cells, incorporating the pristine and g-CNZP–modified LMAs and the Bi-HSE composite electrolyte. Fig. 4(c) compares the EIS spectra of the symmetrical cells, using as-prepared with pristine and g-CNZP composite–modified LMAs. The interfacial resistance of the symmetrical cell prepared with the g-CNZP composite–modified Li metal was much lower than that of the cell featuring pristine Li electrodes. Thus, the presence of the g-CNZP composite coating material on the surface of the Li metal provided better

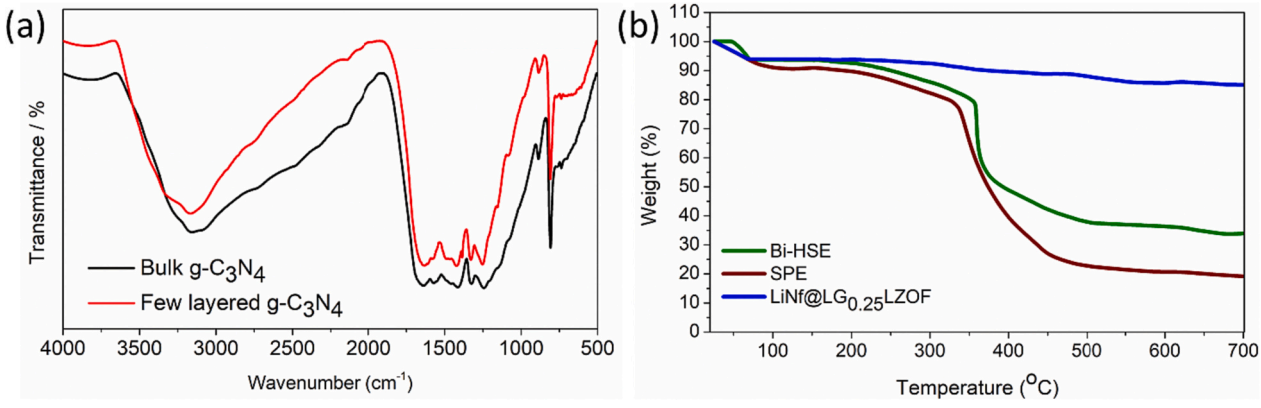

Fig. 3. (a). FTIR spectra of bulk and few-layered g-C_3N_4, (b). TGA curves of LiNf@$LG_{0.25}$LZO powder and the Bi-HSE and SPE membranes.

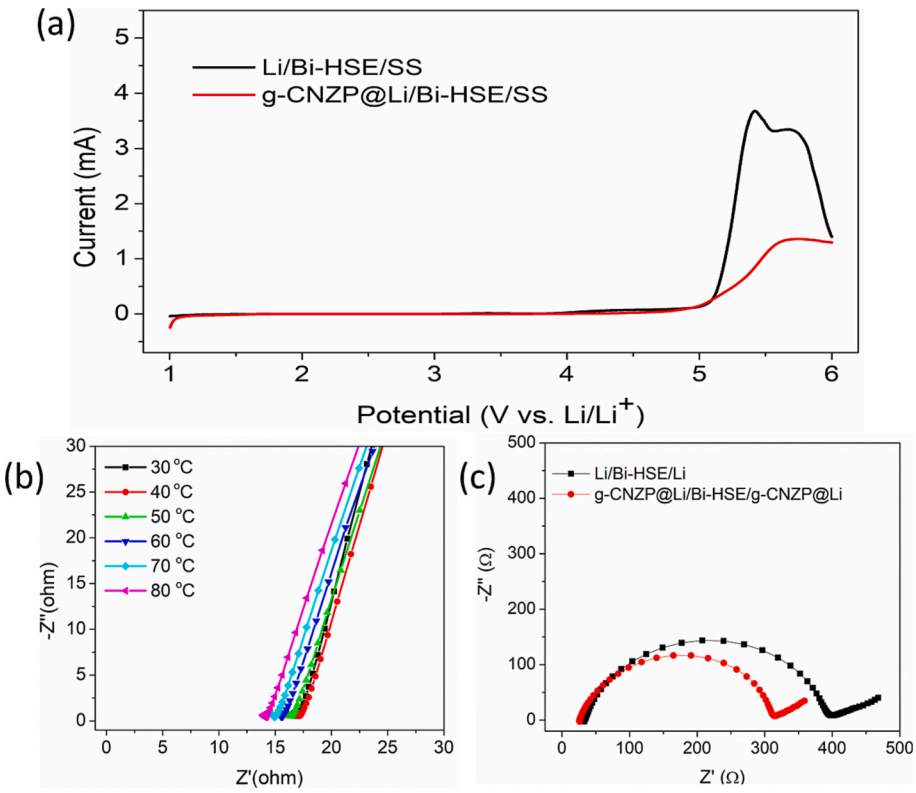

Fig. 4. (a). Linear sweep voltammograms of the Bi-HSE membrane assembled with pristine (Li/Bi-HSE/SS) and modified Li (g-CNZP@Li/Bi-HSE/SS) metal anode recorded at a scan rate of 1 mV s^{-1}, (b). Ionic conductivity of Bi-HSE composite membrane measured at different temperatures, at 30–80 °C, (c). EIS spectra of pristine and g-CNZP coated Li metal anodes for the symmetric cells.

compatibility and more intimate contact with the Bi-HSE composite electrolyte membrane.

We used X-ray photoelectron spectroscopy (XPS) to study the states of the Li, N, S and F atoms in the pristine and g-CNZP–modified LMAs. After the plating/stripping performance test of the cells (both pristine and modified LMA), the cells were disassembled and subjected to XPS analysis. In Fig. 5(a) the Li 1s XPS spectra exhibited peaks at 56.6, 55.7, and 55.0 eV can be attributed to the formation of LiF, Li_2CO_3, and Li_3N, respectively. It is worth noting that LiOH is also generated on the surface of pristine LMA. However, the intensities of these compounds are relatively lower than those observed for the modified LMA. A strong Li 1s peak appeared at 55.0 eV for the g-CNZP–modified LMA, representing the presence of Li_3N. In contrast, the intensity of Li_3N in pristine LMA is notably lower than that of its modified LMA counterpart. The existence of Li_3N was also confirmed by the variations in the chemical states of the N 1s peak in Fig. 5(b). The main peaks in the N 1s spectrum of the pristine LMA after cycling were located at 400.4 and 398.7 eV, corresponding to the N atoms in the $TFSI^-$ anion and *in situ*–formed Li_3N, respectively. The area intensity of the *in situ*–formed Li_3N at 398.7 eV in the g-CNZP–modified LMA sample was significantly higher than that of the pristine one. The presence of the g-C_3N_4 coating material contributed more to the formation of Li_3N during the electrochemical cycling. The low-intensity peak at 400.4 eV for the g-CNZP–modified LMA arose from the $TFSI^-$ anion; this value was supported by the signal in the S 2p XPS spectrum [Fig. 5(c)] at 167.6 eV, with both coinciding reasonably well with the binding energies expected for the chemical environments of the N and S atoms in the $TFSI^-$ anion. In the S 2p spectrum, a second peak near 161 eV was indicative of reductive Li-salt decomposition; this binding energy is characteristic of S atoms in a zero oxidation state [38].

The presence of a LiF SEI layer on the surface of the cycled LMA was further confirmed by the F 1 s spectra. Fig. 5(d) reveals the appearance of peaks at 686.5 and 686.3 eV for LiF in the pristine and g-CNZP–modified LMA samples, respectively. Furthermore, the presence of peaks near 690 eV in the spectra of both LMAs can be attributed to the C—F interactions that occur within the coating polymer (PVDF) or polymer from the Bi-HSE membrane (PVDF-HFP) and the LiTFSI group. The application of ZIF-8, which possesses nanoscale dimensions, as a component of the composite coating material may serve as a regulator for Li-ion transport, thereby ensuring exceptional diffusion of Li-ions during charge/discharge cycling. Additionally, the inclusion of ZIF-8 nanoparticles might also inhibit the growth of Li dendrites and enhance interfacial contact between the Bi-HSE composite membrane and the LMA, ultimately leading to enhanced long-term cycling performance and stability of the cell at a high cut-off voltage (4.5 V) for high-energy-density LMBs.

We subjected the assembled symmetrical cells to galvanostatic charge/discharge long-term testing to examine the Li plating/stripping behavior of the pristine and g-CNZP–modified LMAs. Fig. 6(a) reveals that the pristine Li/Bi-HSE/Li symmetrical cell starts polarizing after 100 h of cycling at 0.2 mA cm^{-2}. The polarization potential observed at the 12th h is *ca.* 111.2 mV (−118.4 mV). Subsequently, after a duration of 370 h, the cell displayed a polarization of *ca.* 113 mV (−120.3 mV). On the other hand, the modified Li metal is stripped and plated reversibly, and the cell exhibits a stable cycling behavior at 0.2 mA cm^{-2}. The polarization potential of g-CNZP–modified LMA at 12th h is 78.1 mV (−80.1 mV) and after 370th h the cell exhibits a lower polarization of 70.6 mV (−71.4 mV). No obvious change in polarization is observed, indicating excellent interfacial stability between g-CNZP@Li and Bi-HSE membrane. The symmetrical cell containing the g-CNZP–modified LMA and the Bi-HSE provided a very stable polarization voltage for >400 h long-term cycling [insets to Fig. 6(a)]. We conducted an experiment to evaluate the performance of the Li/Bi-HSE/Li and g-CNZP@Li/Bi-HSE/g-CNZP@Li symmetrical cells at different current densities to investigate whether the presence of the g-CNZP composite coating material on the surface of the Li metal could inhibit the formation of Li dendrites and enhance the stability of the low-resistance

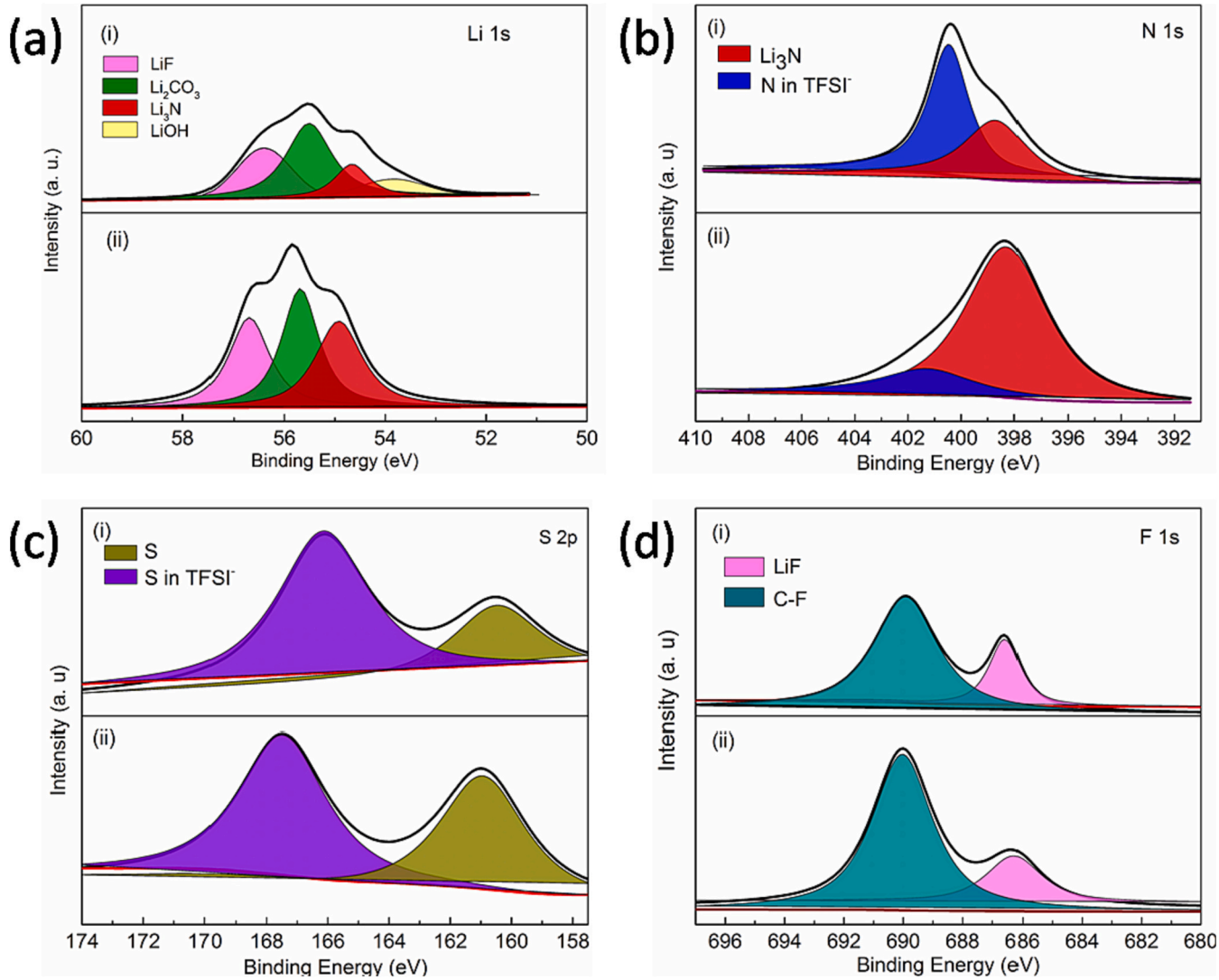

Fig. 5. XPS analysis of (a). Li 1s, (b). N 1s, (c). S 2p, and (d). F 1s for (i) pristine and (ii) g-CNZP-modified LMA after cycling.

interface. During the experiment, the symmetrical Li cells were exposed to a fixed Li plating/stripping time of 2 h for 10 cycles of each current density, while the current densities were varied (*i.e.*, 0.1, 0.2, 0.5, 1.0 and 1.5 mA cm^{-2}) as displayed in Fig. 6(b). The suppression capability of lithium dendrites and interface stability can be reflected by the critical current density (CCD). It is a crucial factor that determines the charge/discharge rate performance of LMBs The good surface contact, high ionic conductivity, and stable interface contribute to the high value of CCD [39]. The pristine Li anode exhibited an increase in polarization voltage upon increasing the current density. In contrast, the cycling of the g-CNZP–coated LMA was relatively stable, with lower polarization potentials up to 1.0 mA cm^{-2} and an overpotential response that closely followed Ohm's law at the various current densities. The polarization voltage of the g-CNZP–coated LMA was approximately 120 mV at 0.5 mA cm^{-2}; the corresponding pristine LMA was highly polarized at the same current density and underwent uneven plating and stripping phenomenon and highly polarized. The excellent behavior of the g-CNZP–coated LMA might have been due to the improved interfacial contact, which enabled rapid transport of Li-ions between the modified LMA and the solid electrolyte membrane, due to the *in-situ* formation of a layer of the Li-ion conductor Li_3N at the interface and the presence of the ZIF-8 nanoparticles (Li-ion transport flux regulator). The presence of Li_3N improved the intimate interfacial contact and caused the local current density to be distributed evenly. Furthermore, the presence of Li_3N, which has negligible electronic conductivity ($\sigma_e < 10^{-12}$ S cm^{-1}), prohibited the conduction of electrons between the Li metal and garnet in the Bi-HSE composite electrolyte [23]. Thus, the presence of composite coating material on our LMA surface could effectively decrease the interfacial resistance and polarization during cycling. As a result, the symmetrical Li cell containing the g-CNZP coating material displayed superior cycling stability and a relatively lower overpotential when compared with those of the cell featuring the pristine LMA. Hence, the electrochemical data suggested that the g-CNZP coating material had potential for use in all-solid-state LMBs (ASSLMBs) displaying high-rate capability and stable long-term cycling electrochemical performance.

We compared the *in-situ* gases released from cells containing the LiNf@NCM811 composite cathode material, both pristine and g-CNZP coated Li metal anode charged at higher cut-off voltage (4.5 V) when featuring the Bi-HSE solid electrolyte and using a liquid electrolyte (LE), comprising of 1 M $LiPF_6$ in ethylene carbonate (EC) and diethyl carbonate (DEC) (1:1, *v*/v). Here, we employed differential electrochemical mass spectrometry (DEMS), which has been used widely to study gas release behavior during *in-situ* charge/discharge processing of rechargeable Li metal batteries. Fig. 7 presents the first three cycles of the charge/discharge curves and the intensity of gas released during cell operation with the solid (LiNf@NCM811/Bi-HSE/Li, LiNf@NCM811/Bi-HSE/g-CNZP@Li) and liquid (LiNf@NCM811/LE/Li) electrolytes. The *in-situ* DEMS measurements of the NCM811/Li cells, featuring Bi-HSE

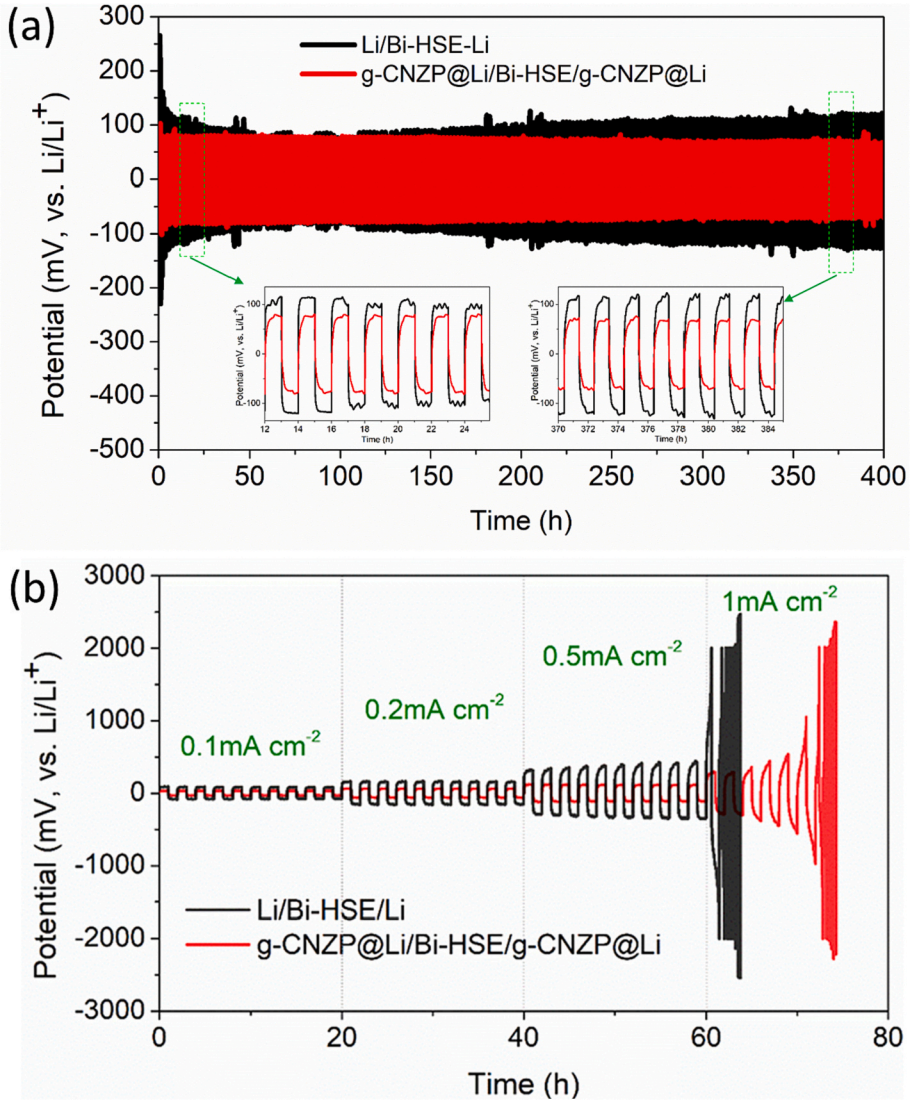

Fig. 6. (a). Galvanostatic cycling curves of Li/Bi-HSE/Li and g-CNZP@Li/Bi-HSE/g-CNZP@Li symmetrical cells at 0.2 mA cm^{-2}; inset: magnified regions at selected time periods, 12–25 h and 370–385 h, (b). Symmetrical cell rate performance test of Li/Bi-HSE/Li and g-CNZP@Li/Bi-HSE/g-CNZP@Li.

and LE allowed the evolution of released gases (*e.g.*, O_2, CO_2, CO, C_2H_4, H_2, C_2H_2, C_2H_6) to be identified qualitatively throughout the electrochemical tests. The ion intensities of the released gases were detected for the LiNf@NCM811/Bi-HSE/Li, LiNf@NCM811/Bi-HSE/g-CNZP@Li and LiNf@NCM811/LE/Li cells when operated between 2.7 and 4.5 V. The gases listed above were detected to greater extents from the cells containing the LE than that of from those featuring the Bi-HSE solid electrolyte. Large amounts of C_2H_4 and CO were generated, through the decomposition of EC (Fig. S3), as the main gas products from the EC-containing electrolyte. Presumably, severe redox reactions resulted in the decomposition of EC (see the Supporting Information) [40]. Figs. 7 and S4 reveal that, with the exception of H_2, all of the gases emitted from the LE-based LiNf@NCM811/Li cell were higher intensities than those of the cell from the Bi-HSE membrane counterpart. We suspect that moisture absorbed by the as-prepared composite membrane electrolyte during punching and cell assembly was responsible for the increase in H_2 production from the cell containing the Bi-HSE membrane. The gas intensities observed at higher cut-off voltages for the cell that contains the Bi-HSE solid electrolyte membrane (both pristine and coated Li cells) were found to be lower, as compared to that of the LE cell. This can be attributed to the inert nature of the Bi-HSE membrane, which hinders any potential redox reactions within the composite membrane components or between the electrode materials. This finding is further corroborated by the LiNf@NCM811/Bi-HSE/g-CNZP@Li cell, where the ion intensities of gas formation are also lower than its pristine counterpart. This could possibly be attributed to the protective effect of the g-CNZP composite coating material on the Bi-HSE membrane. The coating material acts as a barrier, preventing direct contact between the Li metal anode and Bi-HSE, thus mitigating the decomposition of polymer materials and other potential side reactions. Furthermore, such coating material can adjust their strength through a change in strain, thereby accommodating Li deformation and hindering the occurrence of side reactions. The inclusion of inorganic protective filler materials (g-C_3N_4 and ZIF-8) possesses high mechanical moduli and fast Li^+ ion diffusion coefficients. Therefore, our design of the Bi-HSE membrane with modification of the Li metal anode allows for the optimal utilization of each component in the HSE and enhances the electrochemical performance of high-voltage solid-state LMBs.

3.2. *Electrochemical performance of LiNf@NCM811/Bi-HSE/g-CNZP@Li cell*

We investigated the stability and cell performance of the LiNf@NCM811 cathode and g-CNZP@Li with the Bi-HSE composite

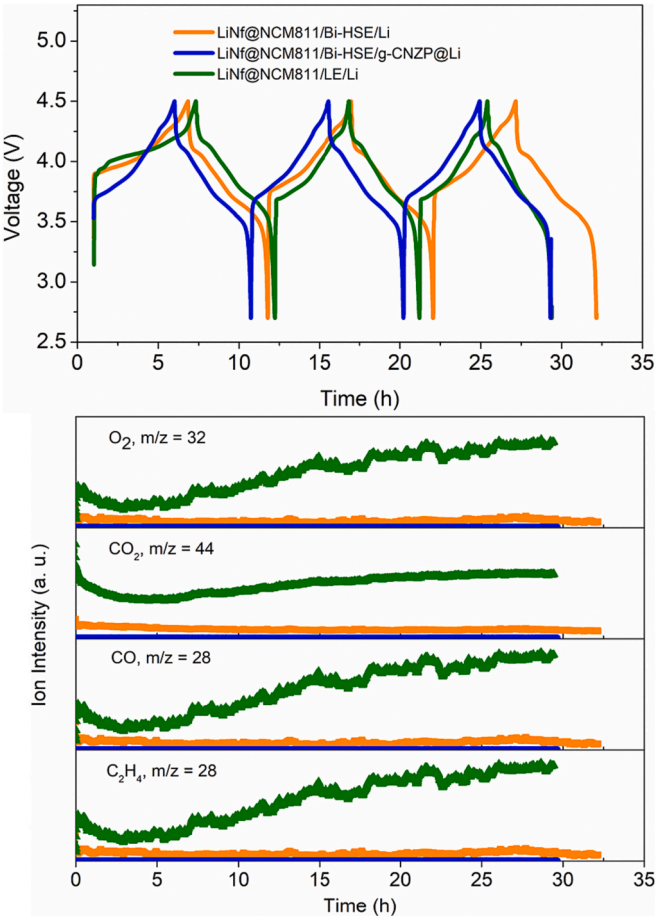

Fig. 7. Voltage profile and the corresponding gas generations (O_2, CO_2, CO and C_2H_4) as a function of the electrochemical cycling of the pristine (LiNf@NCM811/Bi-HSE/Li), modified lithium (LiNf@NCM811/Bi-HSE/g-CNZP@Li) and pristine Li with liquid electrolytes (LiNf@NCM811/LE/Li, where LE is 1 M $LiPF_6$ in EC/DEC 1:1, *v*/v). *m/z* is the mass to charge ratio of the specific gaseous molecules.

electrolyte. We galvanostatically charged and discharged the fabricated LiNf@NCM811/Bi-HSE/g-CNZP@Li cells between 2.8 and 4.2 V (4.5 V) at 30 °C and room temperature. Fig. 8(a) reveals that the cell incorporating the g-CNZP@Li exhibited very stable long-term cycling for >280 cycles at a charging rate of 0.5C at 30 °C. After the first three cycles of the formation step at 0.1C, the cell prepared with the modified LMA exhibited an initial specific capacity of 134.5 mAh g^{-1} at a rate of 0.5C with a retention of 86.1 % after 280 cycles. The average coulombic efficiency of the cell is approximately 99.8 %. In contrast, the pristine LMA assembled with Bi-HSE membrane displayed lower stability and poor interfacial contact. The pristine Li metal anode cell (LiNf@NCM811/Bi-HSE/Li) runs only 110 cycles with an average coulombic efficiency of 97.8 % and the cell dead due to short circuit.

Fig. 8(b) displays the charge/discharge profile of the cell containing the modified LMA. The pristine and modified LMA were also charged between 2.8 and 4.5 V at a rate of 0.2C at room temperature. The long-term cycling performance is shown in Fig. 8(c). The modified LMA delivered an initial specific discharge capacity of 194.4 mAh g^{-1}. After 100 cycles, the battery retained a specific discharge capacity of 162.3 mAh g^{-1}, with a capacity retention of 81.8 % (the fourth cycle provided the maximum specific capacity, 198.5 mAh g^{-1}). The corresponding charge-discharge profile for the modified LMA charged between 2.8 and 4.5 V is displayed in Fig. 8(d). We ascribe this behavior to the excellent interfacial stability of the g-CNZP–coated LMA with the solid-state electrolyte membrane, leading to highly reversible Li-ion extraction and insertion. In contrast, the cell featuring the pristine LMA exhibited poor stability and rapid capacity fading. To investigate the interfacial compatibility of the surfaces of the modified and pristine LMAs with the solid-state electrolyte membrane, we performed EIS testing for cells at high voltage (4.5 V) before and after cycling, between a frequency range from 1 MHz to 100 mHz [Fig. 8(e) and (f)]. The charge-transfer resistance (R_{ct}) of the fresh cell containing the g-CNZP–coated LMA (*ca.* 228 Ω) was lower than that of the cell featuring the pristine LMA (398.5 Ω), this is due to an intimate contact between the modified LMA and the Bi-HSE composite membrane surface.

After 100 cycles, we observed a semicircle at higher frequency, derived from SEI impedance, due to the passage of ions on the anode surface (R_{SEI}), and a second semicircle in the intermediate-frequency region representing the R_{ct} impedance between the electrode and the electrolyte. Fig. 8(e) and (f) reveal that the values of R_{SEI} and R_{ct} of the g-CNZP–modified LMA cell were significantly lower than those of the cell containing the pristine LMA. Thus, after the long-term cycling, the composite coating material formed a more stable interfacial layer with the composite membrane than did the counterpart cell featuring the pristine LMA, such that the former ASSLMBs possessed better cycle stability. We attribute the improved cycle behavior to the enhanced electrochemical performance resulting from the presence of 2D graphitic-C_3N_4 nanosheet, ZIF-8 nanoparticle and polymeric (PVDF) coating layer, which ensured superior interfacial contact at the electrolyte–electrode interface.

We suggest the following reasons for the improved and more-stable electrochemical performance of the g-CNZP@Li/Bi-HSE/LiNf@NCM811 cells at higher cut-off voltages. (i) The nanosheet/nanoparticle structure of g-C_3N_4/ZIF-8/PVDF suppressed Li dendrite formation, improved the Li-ion diffusion, and provided intimate contact with the Bi-HSE membrane; (ii) The high amount of LLZO filler (80 wt% filler *vs.* polymer) on the Li anode side enhanced the mechanical strength of the composite membrane and further inhibits the growth of Li dendrites; (iii) Long-term charge/discharge cycling at a high cut-off voltage 4.2 (4.5 V) led to the *in-situ* formation of Li_3N from the g-CNZP coating material, particularly from the decomposition of 2D g-C_3N_4 nanosheet layer as determined through XPS analysis of the coated Li metal; the *in situ*–formed Li_3N had good Li-ion ionic conductivity and leads to the formation of a stable SEI layer at the g-CNZP@Li–Bi-HSE interface; it can ensure superior performance at a high cut-off voltage of 4.2 (4.5 V) [41].

3.3. Postmortem analysis of the composite membrane and g-CNZP modified Li anode

To understand the various electrochemical performances of ASSLMBs that contains the Bi-HSE membrane and modified LMA, the g-CNZP@Li/Bi-HSE/g-CNZP@Li symmetrical cells that had been operated at different current densities were disassembled [Fig. 9(a)–(d)]. Fig. 9(e) and (f) display the disassembled LiNf@NCM811/Bi-HSE/g-CNZP@Li full cells after long-term electrochemical performance testing at 0.2C between 2.8 and 4.5 V at room temperature. Fig. 9(a) and (b) present the pristine and modified LMAs of the disassembled symmetrical cells, while Fig. 9(c) and (d) present SEM images of the bilayer hybrid composite membrane surfaces after cycling. The presence of a void volume on the surface of the Bi-HSE composite membrane assembled with the pristine Li anode might have been due to uneven plating and stripping during long-term cycling [Fig. 9(c)]. This result is further supported from the change in polarization of the pristine LMA symmetry cell cycling. This phenomenon caused the growth of Li dendrites on the surface of the cycled pristine Li metal, as evidenced by the appearance of cracks on the surface of the pristine Li metal [Fig. 9(a)]. In contrast, the surfaces of the Bi-HSE composite membranes assembled with the g-CNZP@Li and LiNf@NCM811 metal anodes were planar and relatively smooth; it is due to the effect of the artificial SEI layer (ASEI) of the g-CNZP composite coating material (g-C_3N_4/ZIF-8/PVDF) [Fig. 9(d) and (f),

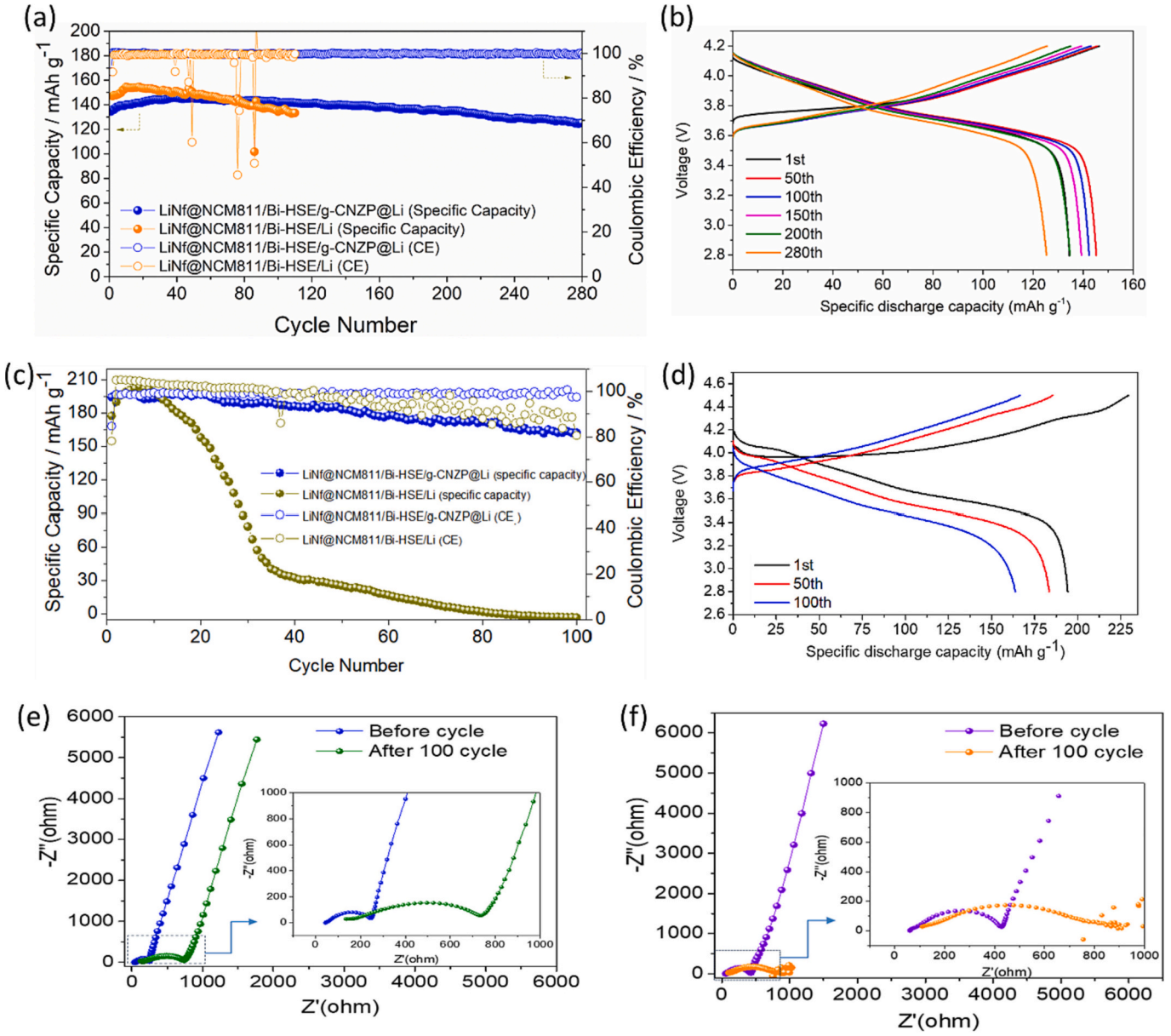

Fig. 8. Comparison of Long-term cycling stability of the LiNf@NCM811/Bi-HSE/g-CNZP@Li and LiNf@NCM811/Bi-HSE/Li cell (a). Charged between 2.8 and 4.2 V at 30 °C, at a rate 0.5C, (b). Charge/discharge voltage profile of the LiNf@NCM811/Bi-HSE/g-CNZP@Li cell between 2.8 and 4.2 V, (c) long-term cycling performance at 0.2C, measured between 2.8 and 4.5 V at room temperature, (d). corresponding charge/discharge voltage profile of the cells. EIS plots of (e). LiNf@NCM811/Bi-HSE/g-CNZP@Li, (f). LiNf@NCM811/Bi-HSE/Li cell before and after 100 cycles, charged between 2.8 and 4.5 V at room temperature.

respectively]. Similarly, the composite coating particles that had been deposited on the surfaces of the Li metal in the symmetrical cell and the full cell potentially suppressed the formation of Li dendrites [Fig. 9(b) and (e)]. The excellent electrochemical performance phenomena suggests that the coating material would provide good mechanical strength and support to Bi-HSE composite membranes in high-voltage ASSLMBs. Moreover, long-term cycling led to the *in-situ* formation of Li_3N, which is a good Li-ion conductor [42] that also enabled a stable interface [23] to exist between the g-CNZP@Li metal and the Bi-HSE composite membrane. Therefore, our composite coating material provided good interfacial contact by decreasing the impedance of the cell, while also being compatible with the composite membrane surface.

Moreover, an overview of the electrochemical characteristics of the Bi-HSE membrane and the cells incorporating modified LMA is presented in Table 1. Notably, the modified Li anode displayed a remarkable performance at high cut-off voltages in comparison to previously reported literature results for nickel-rich cathode materials. The presence of an inorganic/organic composite coating material on the Li metal surface enhances interfacial contact, promotes *in-situ* formation of Li-ion conducting compounds, and impedes Li dendrite growth. These factors facilitate the sustained long cycling of the cell at high cut-off voltage (4.5 V), leading to the achievement of a high-energy density Li metal battery over an extended period.

4. Conclusions

We have prepared a few-layered 2D g-C_3N_4 filler through the calcination of melamine and obtained an artificial SEI (ASEI) layer from a mixed coating material g-C_3N_4/ZIF-8/PVDF (g-CNZP) applied to the surface of an LMA. The presence of the 2D nanosheet layered morphology and ZIF-8 nanoparticle with PVDF binder improved the interfacial contact by creating a compatible environment between the

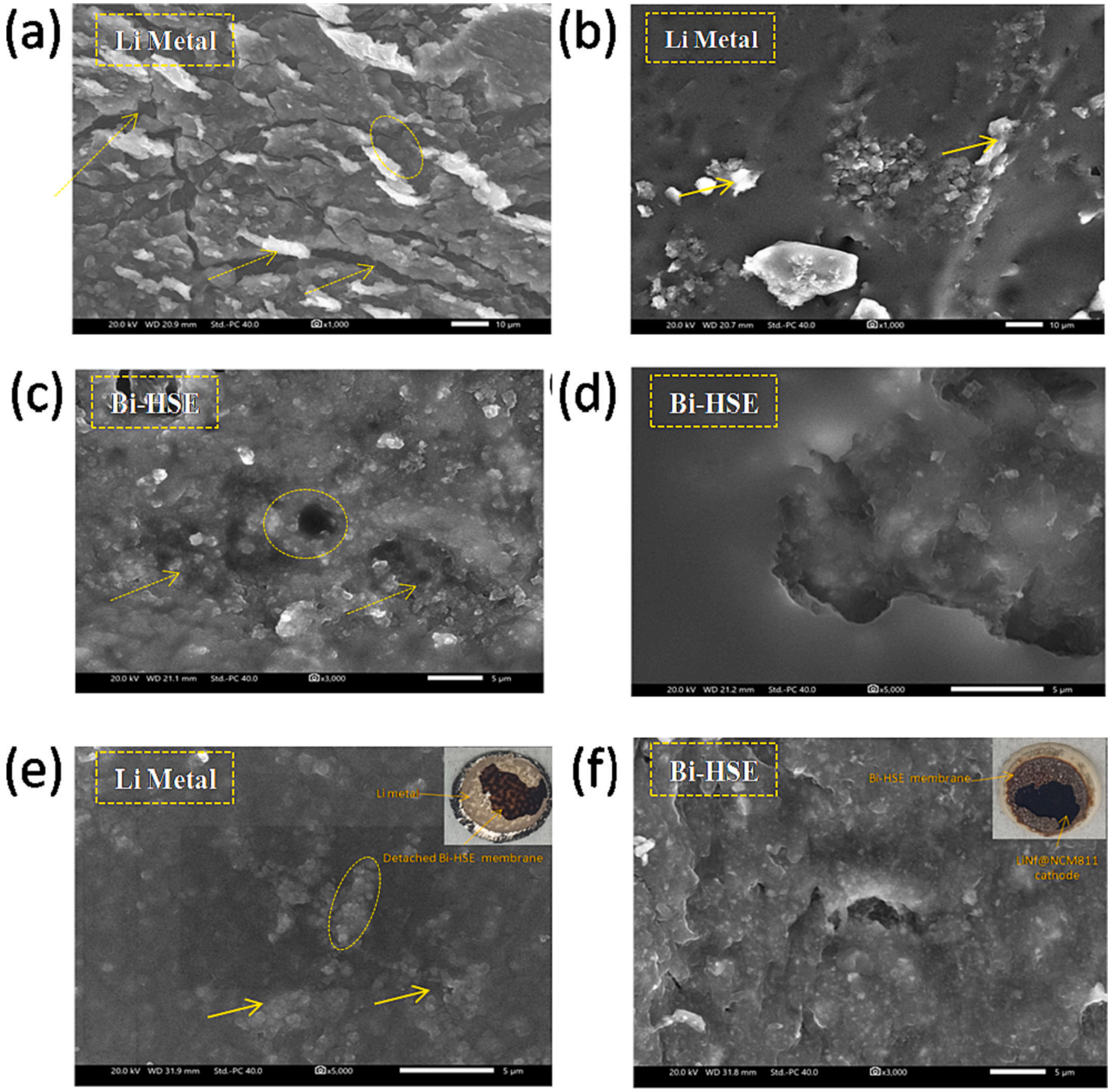

Fig. 9. SEM surface images of Li metal after symmetry cell performance test (a). Pristine Li, and (b). g-CNZP coated Li anode; Bi-HSE membrane from symmetry cell cycling performance test with, (c). Pristine Li, and (d). g-CNZP coated Li anode; (e). g-CNZP@Li metal surface from LiNf@NCM811/Bi-HSE/g-CNZP@Li coin cell (the inset photographic image of Li metal), and (f). Bi-HSE composite membrane (the inset photographic image of Bi-HSE) from LiNf@NCM811/Bi-HSE/g-CNZP@Li coin cell after cycling at 0.2C between 2.8 and 4.5 V at room temperature.

composite membranes and the LMA and suppressing Li dendrite formation during long-term cycling. The g-CNZP@Li/Bi-HSE/LiNf@NCM811 full cell charged from 2.8 to 4.2 V (4.5 V) displayed enhanced electrochemical performance, due to the 2D nanosheet structure of the g-C_3N_4 and ZIF-8 nanoparticles (Li-ion transport flux regulator) in PVDF polymer, which suppressed dendrite formation on the surface of the Li anode. Furthermore, the presence of a large amount of as-prepared ceramic LiNf@$LG_{0.25}$LZOF fillers (80 wt% filler *vs.* polymer) on the modified Li anode side provided the composite membrane (so-called Polymer-in-Ceramic, PIC structure) with better mechanical stability. Long-term cycling at a high cut-off voltage led to *in-situ* formation of Li_3N from the g-CNZP coating material on the LMA, as determined through XPS analysis. This Li_3N had good ionic conductivity, and the formation of a stable SEI layer at the g-CNZP@Li–Bi-HSE interface led to superior performance at the high cut-off voltage of 4.2 V (or 4.5 V). Thus, our as-prepared bilayer-structured HSE and artificial SEI layer on the Li anode appear to have highly potential for use in high-safety and high-energy-density ASSLMBs.

CRediT authorship contribution statement

Methodology & Data Curation: Kumlachew Zelalem Walle, Yi-Shiuan Wu

Data Analysis: All authors

Table 1
Literature report on electrochemical performance of SSE charged at high voltage of 4.5 V.

Cell formulation	ESWs (V *vs.* Li/Li^+)	σ_t (mS cm^{-1})	SSE thickness (μm)	Capacity retention (%)	Electrochemical performance	Ref.
LiNf@NCM811/Bi-HSE/ g-CNZP@Li	5.0	0.68 @25 °C	140–150	81.8 86.1	Initial 194.3 mAh g^{-1}, 100 cycles, 2.8–4.5 V, at 0.2C Initial 134.45 mAh g^{-1}, 280 cycles, 2.8–4.2 V, at 0.5C	This work
Li|SPE|$LiNi_{0.5}Co_{0.2}Mn_{0.3}O_2$	5.1	1.3 @25 °C	~100	~90	Initial 164.2 mAh g^{-1}, 200 cycle, 2.8–4.5 V, at 0.5C	[43]
NCM811/SSCE/Li	5.0	0.51	N/A	N/A	Initial ~150 mAh g^{-1}, 42 cycle, 3.0–4.5 V, at 0.1C	[44]
Li_2MoO_4@$LiN_{0.8}C_{0.1}M_{0.1}O_2$/HIHSE/Li full	4.9	0.28 @25 °C	325	89.2	Initial ~150 mAh g^{-1}, 100 cycle, 2.6–4.5 V, at 0.1C	[45]
NCM811/trilayer LAGP SSE/Li	5.1 @60 °C	0.11 @60 °C	~260	N/A	Initial ~208 mAh g^{-1}, 1 cycle, 3.0–4.5 V, at 0.1C	[46]

Validation: Wen-Chen Chien, Jeng-Kuei Chang

Manuscript draft, review, edit: Kumlachew Zelalem Walle, Yi-Shiuan Wu, Rajan Jose, and Chun-Chen Yang

Funding acquisition: Chun-Chen Yang

Declaration of competing interest

The authors declare that there is no an official competing interest or personal relationships that could have appeared to influence the work presented in this paper.

Data availability

Data will be made available on request.

Acknowledgments

The authors thank the Ministry of Science and Technology of Taiwan for support through the University-Industry Cooperation Project (grant number MOST 108-3116-F-131-001-CC1 and MOST-111-2221-E131-003). And our sincere gratitude goes to Li-Fan Chen for XPS services at the high-resolution analytical instrumentation center, National Central University.

Appendix A. Supplementary data

Supplementary data to this article can be found online at https://doi.org/10.1016/j.est.2023.109757.

References

[1] C. Sun, J.H. Zhang, X.F. Yuan, J.N. Duan, S.W. Deng, J.M. Fan, J.K. Chang, M. Sen Zheng, Q.F. Dong, ZIF-8-based quasi-solid-state electrolyte for lithium batteries, ACS Appl. Mater. Interfaces 11 (2019) 46671–46677, https://doi.org/10.1021/acsami.9b13712.

[2] S. Li, S.Q. Zhang, L. Shen, Q. Liu, J. Bin Ma, W. Lv, Y.B. He, Q.H. Yang, Progress and perspective of ceramic/polymer composite solid electrolytes for lithium batteries, Adv. Sci. 7 (2020) 1–22, https://doi.org/10.1002/advs.201903088.

[3] G. Rollo-Walker, N. Malic, X. Wang, J. Chiefari, M. Forsyth, Development and progression of polymer electrolytes for batteries: influence of structure and chemistry, Polymers (Basel) 13 (2021) 1–20, https://doi.org/10.3390/polym13234127.

[4] J.H. Kim, D.H. Park, J.S. Jang, J.H. Shin, M.C. Kim, S.B. Kim, S.H. Moon, S.N. Lee, K.W. Park, High-performance free-standing hybrid solid electrolyte membrane combined with $Li_{6.28}Al_{0.24}La_3Zr_2O_{12}$ and hexagonal-BN for all-solid-state lithium-based batteries, Chem. Eng. J. 446 (2022), 137035, https://doi.org/10.1016/j.cej.2022.137035.

[5] L.W. Tian, J.W. Kim, S.B. Hong, H.H. Ryu, U.H. Kim, Y.K. Sun, D.W. Kim, All-solid-state lithium batteries featuring hybrid electrolytes based on Li^+ ion-conductive $Li_7La_3Zr_2O_{12}$ framework and full-concentration gradient Ni-rich NCM cathode, Chem. Eng. J. 450 (2022), 138043, https://doi.org/10.1016/j.cej.2022.138043.

[6] Y.Y. Sun, Q. Zhang, L. Yan, T.B. Wang, P.Y. Hou, A review of interfaces within solid-state electrolytes: fundamentals, issues and advancements, Chem. Eng. J. 437 (2022), 135179, https://doi.org/10.1016/j.cej.2022.135179.

[7] G. Yu, Y. Wang, K. Li, S. Sun, S. Sun, J. Chen, L. Pan, Z.M. Sun, Plasma optimized $Li_7La_3Zr_2O_{12}$ with vertically aligned ion diffusion pathways in composite polymer electrolyte for stable solid-state lithium metal batteries, Chem. Eng. J. 430 (2022), 132874, https://doi.org/10.1016/j.cej.2021.132874.

[8] M. Liu, X. Guan, H. Liu, X. Ma, Q. Wu, S. Ge, H. Zhang, J. Xu, Composite solid electrolytes containing single-ion lithium polymer grafted garnet for dendrite-free, long-life all-solid-state lithium metal batteries, Chem. Eng. J. 445 (2022), 136436, https://doi.org/10.1016/j.cej.2022.136436.

[9] M. Bai, K. Xie, K. Yuan, K. Zhang, N. Li, C. Shen, Y. Lai, R. Vajtai, P. Ajayan, B. Wei, A scalable approach to dendrite-free lithium anodes via spontaneous reduction of spray-coated graphene oxide layers, Adv. Mater. 30 (2018) 1–7, https://doi.org/10.1002/adma.201801213.

[10] N. Li, W. Wei, K. Xie, J. Tan, L. Zhang, X. Luo, K. Yuan, Q. Song, H. Li, C. Shen, E. M. Ryan, L. Liu, B. Wei, Suppressing dendritic lithium formation using porous media in lithium metal-based batteries, Nano Lett. 18 (2018) 2067–2073, https://doi.org/10.1021/acs.nanolett.8b00183.

[11] W. Luo, Y. Gong, Y. Zhu, K.K. Fu, J. Dai, S.D. Lacey, C. Wang, B. Liu, X. Han, Y. Mo, E.D. Wachsman, L. Hu, Transition from superlithiophobicity to superlithiophilicity of garnet solid-state electrolyte, J. Am. Chem. Soc. 138 (2016) 12258–12262, https://doi.org/10.1021/jacs.6b06777.

[12] Z. Hou, J. Zhang, W. Wang, Q. Chen, B. Li, C. Li, Towards high-performance lithium metal anodes via the modification of solid electrolyte interphases, J. Energy Chem. 45 (2020) 7–17, https://doi.org/10.1016/j.jechem.2019.09.028.

[13] L. Pan, S. Sun, G. Yu, X.X. Liu, S. Feng, W. Zhang, M. Turgunov, Y. Wang, Z.M. Sun, Stabilizing solid electrolyte/Li interface via polymer-in-salt artificial protection layer for high-rate and stable lithium metal batteries, Chem. Eng. J. 449 (2022), 137682, https://doi.org/10.1016/j.cej.2022.137682.

[14] J. Luo, C.C. Fang, N.L. Wu, High polarity poly(vinylidene difluoride) thin coating for dendrite-free and high-performance lithium metal anodes, Adv. Energy Mater. 8 (2018) 1–7, https://doi.org/10.1002/aenm.201701482.

[15] B. Zhu, Y. Jin, X. Hu, Q. Zheng, S. Zhang, Q. Wang, J. Zhu, Poly(dimethylsiloxane) thin film as a stable interfacial layer for high-performance lithium-metal battery anodes, Adv. Mater. 29 (2017) 1–6, https://doi.org/10.1002/adma.201603755.

[16] J. Kang, N. Deng, Y. Liu, Z. Yan, L. Gao, H. Xiang, L. Zhang, G. Wang, B. Cheng, W. Kang, Recent advances of anode protection in solid-state lithium metal batteries, Energy Storage Mater. 52 (2022) 130–160, https://doi.org/10.1016/j.ensm.2022.07.037.

[17] X. Han, Y. Gong, K.K. Fu, X. He, G.T. Hitz, J. Dai, A. Pearse, B. Liu, H. Wang, G. Rublo, Y. Mo, V. Thangadurai, E.D. Wachsman, L. Hu, Negating interfacial impedance in garnet-based solid-state Li metal batteries, Nat. Mater. 1 (2016) 1–9, https://doi.org/10.1038/NMAT4821.

[18] Y. Shao, H. Wang, Z. Gong, D. Wang, B. Zheng, J. Zhu, Y. Lu, Y.S. Hu, X. Guo, H. Li, X. Huang, Y. Yang, C.W. Nan, L. Chen, Drawing a soft Interface: an effective interfacial modification strategy for garnet-type solid-state Li batteries, ACS Energy Lett. 3 (2018) 1212–1218, https://doi.org/10.1021/acsenergylett.8b00453.

[19] P. Hundekar, R. Jain, A.S. Lakhnot, N. Koratkar, Recent advances in the mitigation of dendrites in lithium-metal batteries, J. Appl. Phys. 128 (2020), https://doi.org/10.1063/5.0015099.

[20] M. Bai, K. Xie, B. Hong, K. Zhang, K. Yuan, Z. Huang, J. Zhao, C. Shen, Y. Lai, Surface modification via a nanosized nitride material to stabilize lithium metal anode, Ceram. Int. 45 (2019) 8045–8048, https://doi.org/10.1016/j.ceramint.2019.01.031.

[21] W. Jia, H. Li, Z. Wang, Y. Liu, Y.Y. Yang, J. Li, 3D composite lithium metal with multilevel micro-nano structure combined with surface modification for stable lithium metal anodes, Appl. Surf. Sci. 570 (2021), 151159, https://doi.org/10.1016/j.apsusc.2021.151159.

[22] D. Kang, D. Jin, J. Moon, C.B. Dzakpasu, H. Lee, S. Choi, T. Jo, H. Lee, S.Y. Ryou, Y. M. Lee, $AgNO_3$-preplanted Li metal powder electrode: preliminary formation of lithiophilic ag and a Li_3N-rich solid electrolyte interphase, Chem. Eng. J. 452 (2023), 139409, https://doi.org/10.1016/j.cej.2022.139409.

[23] Y. Huang, B. Chen, J. Duan, F. Yang, T. Wang, Z. Wang, W. Yang, C. Hu, W. Luo, Y. Huang, Graphitic carbon nitride (g-C_3N_4): an Interface enabler for solid-state lithium metal batteries, Angew. Chemie - Int. Ed. 59 (2020) 3699–3704, https://doi.org/10.1002/anie.201914417.

[24] X. Qi, D. Cai, X. Wang, X. Xia, C. Gu, J. Tu, Ionic liquid-impregnated ZIF-8/polypropylene solid-like electrolyte for dendrite-free lithium-metal batteries, ACS

Appl. Mater. Interfaces 14 (2022) 6859–6868, https://doi.org/10.1021/acsami.1c23034.
[25] Q. Zhang, Q. Wang, S. Huang, Y. Jiang, Z. Chen, Preparation and electrochemical study of PVDF-HFP/LATP/g-C_3N_4 composite polymer electrolyte membrane, Inorg. Chem. Commun. 131 (2021), 108793, https://doi.org/10.1016/j.inoche.2021.108793.
[26] Z. Sun, Y. Li, S. Zhang, L. Shi, H. Wu, H. Bu, S. Ding, G-C_3N_4 nanosheets enhanced solid polymer electrolytes with excellent electrochemical performance, mechanical properties, and thermal stability, J. Mater. Chem. A 7 (2019) 11069–11076, https://doi.org/10.1039/c9ta00634f.
[27] W. Zhang, Y. Ma, X. Zhu, L. Wang, J. Ye, X. Hou, S. Liu, M. Lu, H. Tian, X. Hu, In situ synthesis of α-Fe_2O_3/$LaFeO_3$ modified with g-C_3N_4 and Ti_3C_2 for construction of multiple Z-scheme/Schottky heterojunctions as an efficient visible-light photocatalyst for Cr (VI) reduction and organic pollutants removal, J. Alloys Compd. 913 (2022), 165217, https://doi.org/10.1016/j.jallcom.2022.165217.
[28] L. Tan, J. Xu, X. Zhang, Z. Hang, Y. Jia, S. Wang, Synthesis of g-C_3N_4 /CeO_2 nanocomposites with improved catalytic activity on the thermal decomposition of ammonium perchlorate, Appl. Surf. Sci. 356 (2015) 447–453, https://doi.org/10.1016/j.apsusc.2015.08.078.
[29] Z. Zhang, J. Wang, H. Ying, S. Zhang, P. Huang, Z. Zhang, H. Xie, G. Han, W. Q. Han, The role of active passivated interface in poly (ethylene oxide) electrolyte for 4.2 V solid-state lithium metal batteries, Chem. Eng. J. 451 (2023), https://doi.org/10.1016/j.cej.2022.138680.
[30] W. Xu, X. Pei, C.S. Diercks, H. Lyu, Z. Ji, O.M. Yaghi, A metal-organic framework of organic vertices and polyoxometalate linkers as a solid-state electrolyte, J. Am. Chem. Soc. 141 (2019) 17522–17526, https://doi.org/10.1021/jacs.9b10418.
[31] K.Z. Walle, Y.-S. Wu, S.-H. Wu, J.-K. Chang, R. Jose, C.-C. Yang, Lithium nafion–modified $Li_{6.05}Ga_{0.25}La_3Zr_2O_{11.8}F_{0.2}$ trilayer hybrid solid electrolyte for high-voltage cathodes in all-solid-state lithium-metal batteries, ACS Appl. Mater. Interfaces 14 (2022) 15259–15274, https://doi.org/10.1021/acsami.2c00753.
[32] N.A.H.M. Nordin, A.F. Ismail, A. Mustafa, P.S. Goh, D. Rana, T. Matsuura, Aqueous room temperature synthesis of zeolitic imidazole framework 8 (ZIF-8) with various concentrations of triethylamine, RSC Adv. 4 (2014) 33292–33300, https://doi.org/10.1039/c4ra03593c.
[33] K.Z. Walle, L.M. Babulal, S.H. Wu, W. Chien, R. Jose, S.J. Lue, J. Chang, C. Yang, Electrochemical characteristics of a polymer/garnet trilayer composite electrolyte for solid-state lithium-metal batteries, ACS Appl. Mater. Interfaces 13 (2021) 2507–2520, https://doi.org/10.1021/acsami.0c17422.
[34] X. Yu, A. Manthiram, A review of composite polymer-ceramic electrolytes for lithium batteries, Energy Storage Mater. 34 (2021) 282–300, https://doi.org/10.1016/j.ensm.2020.10.006.
[35] F. Fina, S.K. Callear, G.M. Carins, J.T.S. Irvine, Structural investigation of graphitic carbon nitride via XRD and neutron diffraction, Chem. Mater. 27 (2015) 2612–2618, https://doi.org/10.1021/acs.chemmater.5b00411.
[36] J. Lu, Y. Liu, P. Yao, Z. Ding, Q. Tang, J. Wu, Z. Ye, Hybridizing poly(vinylidene fluoride-co-hexafluoropropylene) with $Li_{6.5}La_3Zr_{1.5}Ta_{0.5}O_{12}$ as a lithium-ion electrolyte for solid state lithium metal batteries, Chem. Eng. J. 367 (2019) 230–238, https://doi.org/10.1016/j.cej.2019.02.148.
[37] X. Zhang, T. Liu, S. Zhang, X. Huang, B. Xu, Y. Lin, B. Xu, L. Li, C. Nan, Y. Shen, Synergistic coupling between $Li_{6.75}La_3Zr_{1.75}Ta_{0.25}O_{12}$ and poly(vinylidene fluoride) induces high ionic conductivity, mechanical strength, and thermal stability of solid composite electrolytes, J. Am. Chem. Soc. 139 (2017) 13779–13785, https://doi.org/10.1021/jacs.7b06364.
[38] J. Maibach, I. Källquist, M. Andersson, S. Urpelainen, K. Edström, H. Rensmo, H. Siegbahn, M. Hahlin, Probing a battery electrolyte drop with ambient pressure photoelectron spectroscopy, Nat. Commun. 10 (2019) 1–7, https://doi.org/10.1038/s41467-019-10803-y.
[39] Y. Li, S. Guo, Z. Cao, J. Liu, L. Wang, G. Li, High ionic conductivity and critical current density of $Li_{7-x}La_{2.95}Yb_{0.05}Zr_{2-x}Ta_xO_{12}$ solid electrolyte by modulation of Li^+ distribution, J. Eur. Ceram. Soc. (2023), https://doi.org/10.1016/j.jeurceramsoc.2023.10.052.
[40] X. Teng, C. Zhan, Y. Bai, L. Ma, Q. Liu, C. Wu, F. Wu, Y. Yang, J. Lu, K. Amine, In situ analysis of gas generation in lithium-ion batteries with different carbonate-based electrolytes, ACS Appl. Mater. Interfaces 7 (2015) 22751–22755, https://doi.org/10.1021/acsami.5b08399.
[41] Y. Sun, Y. Li, J. Sun, Y. Li, A. Pei, Y. Cui, Stabilized Li_3N for efficient battery cathode prelithiation, Energy Storage Mater. 6 (2016) 119–124, https://doi.org/10.1016/j.ensm.2016.10.004.
[42] D. Cao, X. Sun, Q. Li, A. Natan, P. Xiang, H. Zhu, Lithium dendrite in all-solid-state batteries: growth mechanisms, suppression strategies, and characterizations, Matter 3 (2020) 57–94, https://doi.org/10.1016/j.matt.2020.03.015.
[43] L. Tang, B. Chen, Z. Zhang, C. Ma, J. Chen, Y. Huang, F. Zhang, Q. Dong, G. Xue, D. Chen, C. Hu, S. Li, Z. Liu, Y. Shen, Q. Chen, L. Chen, Polyfluorinated crosslinker-based solid polymer electrolytes for long-cycling 4.5 V lithium metal batteries, Nat. Commun. 14 (2023), https://doi.org/10.1038/s41467-023-37997-6.
[44] X. Lin, C. Chu, Z. Li, T. Zhang, J. Chen, R. Liu, P. Li, Y. Li, J. Zhao, Z. Huang, X. Feng, Y. Xie, Y. Ma, A high-performance, solution-processable polymer/ceramic/ionic liquid electrolyte for room temperature solid-state Li metal batteries, Nano Energy 89 (2021), https://doi.org/10.1016/j.nanoen.2021.106351.
[45] S.L. Beshahwured, T.H. Mengesha, L.M. Babulal, Y.S. Wu, S.H. Wu, J.K. Chang, R. Jose, C.C. Yang, Hierarchical interconnected hybrid solid electrolyte membrane for all-solid-state lithium-metal batteries based on high-voltage NCM811 cathodes, ACS Appl. Energy Mater. 5 (2022) 2580–2595, https://doi.org/10.1021/acsaem.2c00046.
[46] Z. Zhang, S. Chen, X. Yao, P. Cui, J. Duan, W. Luo, Enabling high-areal-capacity all-solid-state lithium-metal batteries by tri-layer electrolyte architectures, Energy Storage Mater. 24 (2020) 714–718, https://doi.org/10.1016/j.ensm.2019.06.006.